

Introduction to an FBG-based inclinometer and its application to landslide monitoring

Y. L. Wang¹ · B. Shi¹ · T. L. Zhang² · H. H. Zhu^{1,3} · Q. Jie¹ · Q. Sun²

Received: 15 January 2015/Revised: 6 April 2015/Accepted: 17 June 2015/Published online: 31 July 2015
© Springer-Verlag Berlin Heidelberg 2015

Abstract This paper presents a self-designed in-place inclinometer based on fiber Bragg grating (FBG) technology and introduces its application to a landslide monitoring project in Wenzhou, China. The working principle of the FBG-based inclinometer is briefly introduced. The FBG-based inclinometers were installed into nine boreholes that were distributed over different areas of the landslide. After 4 months of monitoring, the deformation of the soil mass at different depths above the bedrock within the landslide was captured by the inclinometers. The results indicated that the soil deformation above the bedrock was relatively large whereas that below the bedrock was minor. Based on the field monitoring data, the potential sliding zones were predicted to be the areas near the bedrock. In addition, a limit equilibrium analysis was carried out to evaluate the stability of the landslide under the circumstance of rainfall. The analyses showed that the calculated failure surface was consistent with the field observations, indicating that the monitoring data recorded by FBGs were accurate. These findings demonstrate that a combination of FBG technique and limit equilibrium analysis can be used to evaluate the stability of landslides effectively.

Keywords Landslide · FBG · Inclinometer · Limit equilibrium analysis (LEA) · Stability assessment

1 Introduction

Field monitoring is an indispensable method to landslide prediction and early warning. Conventional monitoring methods, such as electric-based inclinometers, are the most common instruments to measure subsurface displacements, and have already been widely used in slope monitoring projects. However, these conventional inclinometers have a number of disadvantages in practical applications, including low stability and durability, poor resistance to electromagnetic interference, high gravity dependence, and great signal loss for long-distance transmission. Recently, the fiber optic sensing technologies have been advocated for slope monitoring by some scholars [1–8]. Different types of FBG-based in-place inclinometers have been developed, which demonstrated various features, such as small size, superior chemical resistance and stability, immune to electro-magnetic interference, and quasi-distributed monitoring capability [9–13]. This technology is especially suitable for automatic and long-distance monitoring in landslides.

This paper designed an FBG-based in-place inclinometer, which can monitor the quasi-distributed deformation of soil mass at different depth. The design, calibration and field installation of these inclinometers are presented in detail. Furthermore, this instrument is successfully applied to monitor the deformation of Wencheng landslide in China. The monitoring data collected in the field are analyzed, together with a parametric limit equilibrium analysis (LEA), and some new understandings of the applicability for FBG technique were found.

✉ B. Shi
shibin@nju.edu.cn

Y. L. Wang
wangyilong337@gmail.com

H. H. Zhu
zhh@nju.edu.cn

¹ School of Earth Sciences and Engineering, Nanjing University, Nanjing 210023, China

² Nanjing Center, China Geological Survey, Nanjing 210016, China

³ State Key Laboratory of Hydraulics and Mountain River Engineering, Sichuan University, Chengdu 610065, China

2 Development of an FBG-based in-place inclinometer for landslide monitoring

2.1 Principle of the FBG sensing technique

FBG is essentially a wavelength-selective filter. An FBG sensor will reflect light that has a central wavelength corresponding to Bragg condition, given by [14]:

$$\lambda_b = 2n_{eff}A \tag{1}$$

where λ_b is the Bragg wavelength that will be reflected back; n_{eff} is the effective refractive index of fiber core; and A is the period of the grating. Lights at other wavelengths will be transmitted without significant attenuation, as shown in Fig. 1 [15].

Strain changes the Bragg wavelength through expansion or contraction of the grating periodicity. Besides, temperature variation affects the Bragg wavelength through thermal expansion and contraction of the grating periodicity. The change in Bragg wavelength λ_b , with strain and temperature, can be expressed as [14]:

$$\Delta\lambda_b = 2n\Lambda \left(\left\{ 1 - \left(\frac{n^2}{2} \right) [P_{12} - \nu(P_{11} - P_{12})] \right\} \varepsilon + \left[\alpha + \frac{\left(\frac{dn}{dT} \right)}{n} \right] \Delta T \right) \tag{2}$$

where n is the refractive index of fiber core; ε is the applied strain; P_{11} and P_{22} are the Pockel’s coefficients of the stress-optic tensor; ν is the Poisson’s ratio; α is the coefficient of thermal expansion of the fiber material (e.g., silica); and ΔT is the temperature change.

The measured strain response at an invariable temperature can be defined by:

$$\frac{1}{\lambda_b} \frac{\delta\lambda_b}{\delta\varepsilon} = 0.78 \times 10^{-6} \mu\varepsilon^{-1} \tag{3}$$

In silica fibers, the thermal response is dominated by the $\frac{dn}{dT}$ effect (change of refractive index with temperature), which accounts for nearly 95 % of the observed shift [14].

The normalized thermal response at a constant strain is:

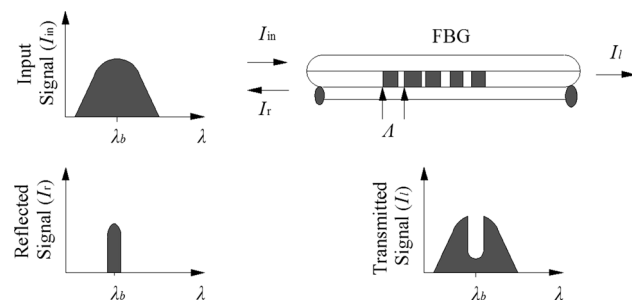


Fig. 1 Transmission and reflection spectra in an FBG

$$\frac{1}{\lambda_b} \frac{\delta\lambda_b}{\delta T} = 6.67 \times 10^{-6} \text{ } ^\circ\text{C}^{-1} \tag{4}$$

Typical values of the dependence of Bragg wavelength on fiber strain and temperature are 1.15 pm/ $\mu\varepsilon$ and 13 pm/ $^\circ\text{C}$, respectively, for an FBG sensor that has a Bragg wavelength of 1550 nm [16]. Since FBGs are sensitive to both strain and temperature, it becomes logical to use them as either strain sensors or temperature sensors or both, and also it is necessary to compensate temperature when strain is only needed.

2.2 Design of the FBG-based in-place inclinometer

In this study, an FBG-based in-place inclinometer with an internal diameter of 7 cm and a thickness of 5 mm was designed and fabricated, as shown in Fig. 2. To meet different engineering requirements and also increase the survival rate of FBGs during field installation, the aluminum inclinometer is divided into several segments (A, B, C, etc.), and each segment is instrumented with an optical fiber with several FBGs connected in series at an interval of 1 m. Then, they are fixed at the opposite side of an aluminum casing in U-shape. The horizontal displacements of the inclinometer can be calculated using the strain measured by the FBG sensors. The inclinometer casing interacts with the surrounding soil mass based on the assumption that the Young’s modulus of the inclinometer casing is consistent with that of the soil. Thus, the FBG-based in-place inclinometer can approximately reflect the internal movement of the monitored slope. The working principle of FBG-based in-place inclinometer is shown in Fig. 3.

According to the classical beam theory, the relationship between the curvature of the inclinometer casing and the applied moment can be expressed by:

$$k = \frac{1}{\rho} = \frac{M}{EI} \tag{5}$$

where k is the inclinometer curvature, ρ is the rotation radius of curvature, M is the pure bending moment applied on the inclinometer casing, E is the Young’s modulus of the inclinometer casing, and I is the moment of inertia. The deflection of inclinometer can be simplified as follows [17]:

$$\Delta f = \frac{(f_{i+1} - f_i)}{h} \tag{6}$$

where f_i is the deflection at the i th FBG sensor position on the inclinometer; f_{i+1} is the deflection at $(i + 1)$ th FBG sensor position on the inclinometer; and h is the distance between two neighboring FBG sensors.

According to the mechanics of materials, the relationship between deflections along the inclinometer casing and

Fig. 2 FBG-based in-place inclinometer

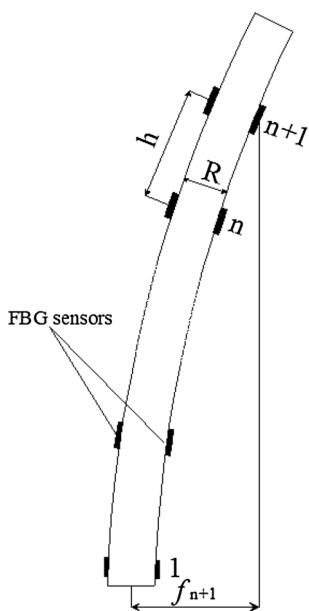
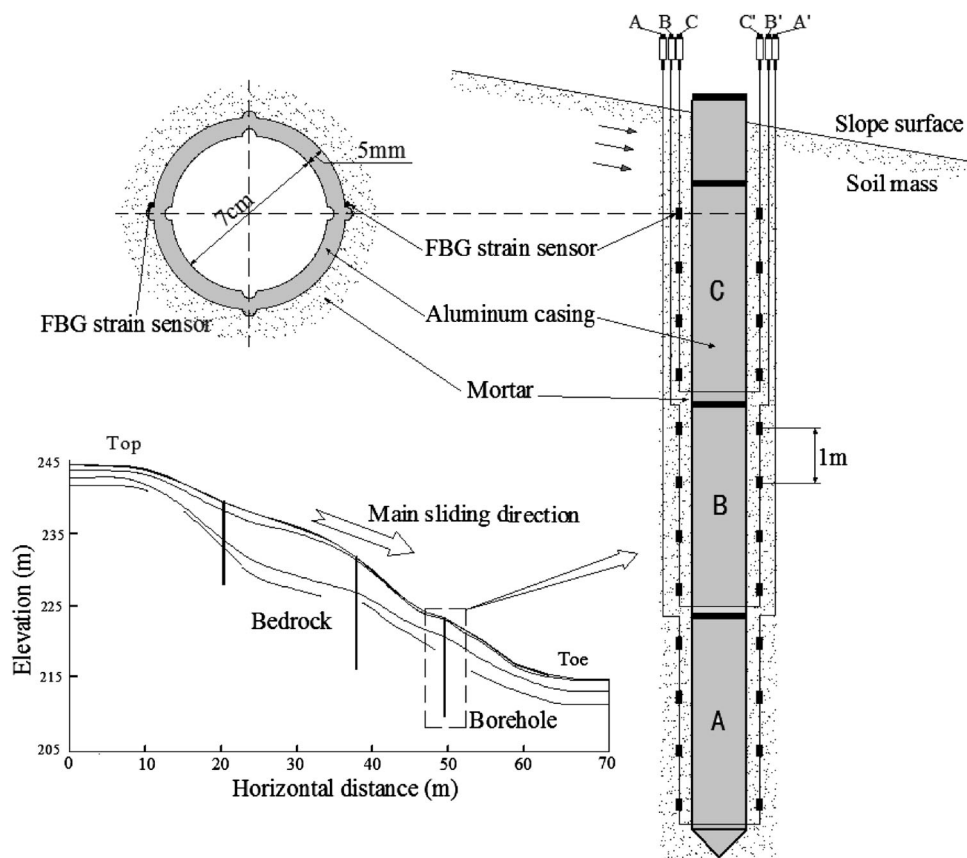


Fig. 3 Working principle of FBG-based in-place inclinometer

the strains measured by FBG strain sensors can be expressed by [17]:

$$\begin{aligned} \Delta(\Delta f) &= \frac{1}{h} \left(\frac{(f_{i+1} - f_i)}{h} - \frac{(f_i - f_{i-1})}{h} \right) \\ &= \frac{1}{h^2} (f_{i+1} - 2f_i + f_{i-1}) = \frac{M}{EI} \end{aligned} \tag{7}$$

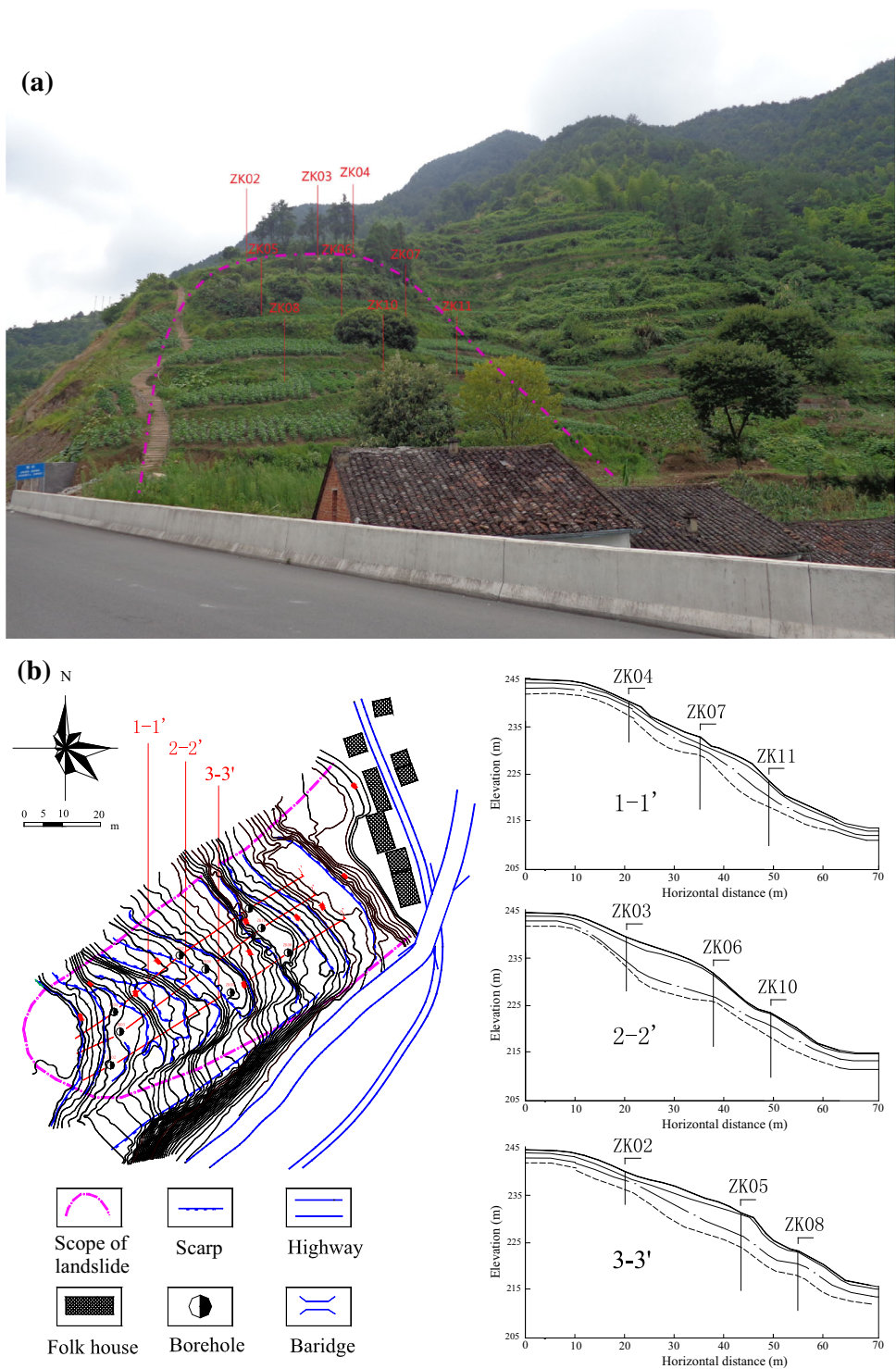
$$\frac{1}{h^2} (f_{i+1} - 2f_i + f_{i-1}) = \frac{1}{R} \frac{MR}{EI} = \frac{\varepsilon_i}{R} \tag{8}$$

where R is the internal diameter of inclinometer; and ε_i is the strain measured by the i th FBG.

The displacement at the bottom of inclinometer is assumed to be zero since the in-place inclinometer is taken as a cantilever. Under such condition, the first two FBG sensors can be neglected because the first two values of the sequence are zero. Thus, the relationship between strain and displacement can be expressed by [17]:

$$\begin{bmatrix} f_2 \\ \vdots \\ f_{n+1} \end{bmatrix} = \frac{h^2}{R} \begin{bmatrix} 1 & 0 & \dots & \dots & \dots & 0 \\ -2 & \dots & \dots & \dots & \dots & \vdots \\ 1 & \dots & \dots & \dots & \dots & \vdots \\ \vdots & \dots & \dots & \dots & \dots & \vdots \\ \vdots & \dots & \dots & \dots & \dots & 0 \\ 0 & \dots & \dots & 1 & -2 & 0 \end{bmatrix}_{n \times n}^{-1} \begin{bmatrix} \varepsilon_1 \\ \vdots \\ \varepsilon_n \end{bmatrix} \tag{9}$$

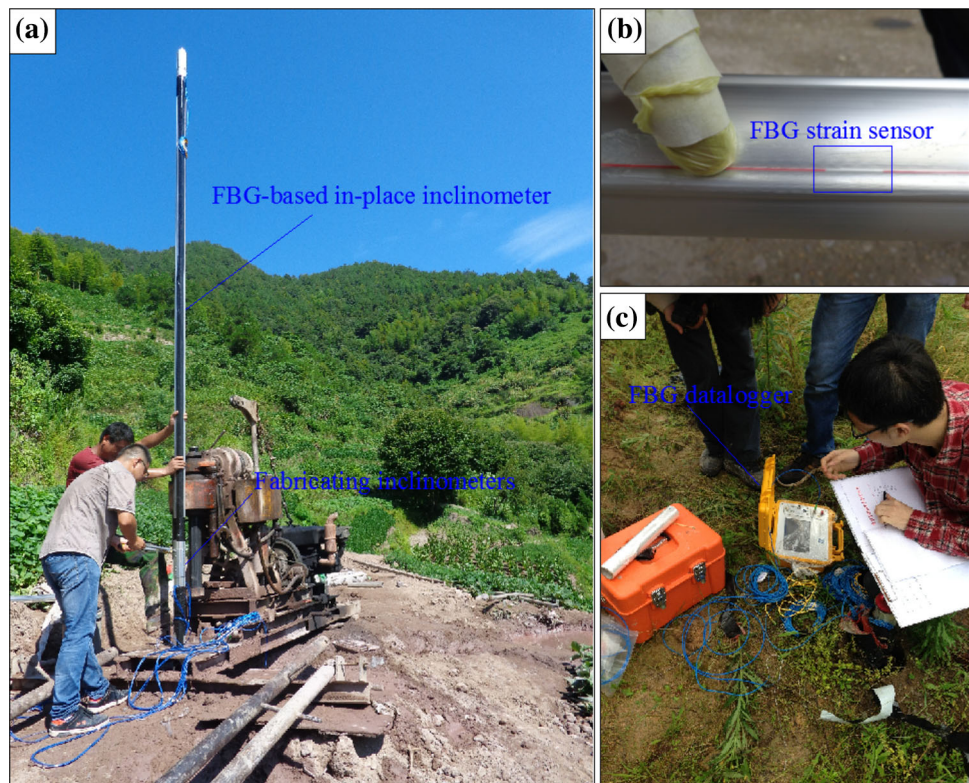
Fig. 4 **a** General view of Wencheng landslide; **b** topographic map of Wencheng landslide



Pei et al. [17] carried out laboratory tests to verify the reliability of the FBG-based inclinometer. Two optical cables multiplexed with FBG strain sensors were fixed at the opposite sides of a PVC beam. The beam was placed horizontal. One end of the beam was fixed and another end was free. In these tests, linear variable displacement

transducers (LVDTs) were employed to measure the vertical displacement at the specialized locations of the beam. Meanwhile, the Bragg wavelengths of FBG sensors were collected using an interrogator. The calculated displacements were compared with the actual displacements measured by LVDTs. The calibration results fit well with the

Fig. 5 **a** Field installation of FBG-based in-place inclinometer; **b** FBG strain sensors fixed on aluminum tube; **c** data acquisition using a NZS-A05 FBG demodulator



LVDTs' measurements with limited errors, which means that this kind of inclinometer is effective and can be applied to monitoring soil mass movements in slope.

3 Monitoring program of Wencheng landslide

To verify the performance of the FBG-based inclinometer in practical slope monitoring project, a landslide (Wencheng landslide) located at Wenzhou, China is selected as a case study area. Figure 4(a) shows the general view of the landslide. The topography of the site is generally high in the southwest, sloping downward at 25° – 30° toward the northeast, with a height of 40 m, as shown in Fig. 4(b). Based on the information of boreholes, the landslide comprises an underlying tuff bedrock and three different weathered degrees of crusts: silty clay, completely weathered tuff, weakly weathered tuff. The soil at landslide surface is used for farming, and some residential constructions are located at the slope toe. The southeast of the slope was excavated during the construction of a highway. On June 19, 2012, several fractures were first noticed by the inhabitants at the landslide crest. The situation threatened the residential area and the highway located at the slope toe.

According to geological condition of the landslide, three typical vertical sections, i.e., 1-1', 2-2' and 3-3', were

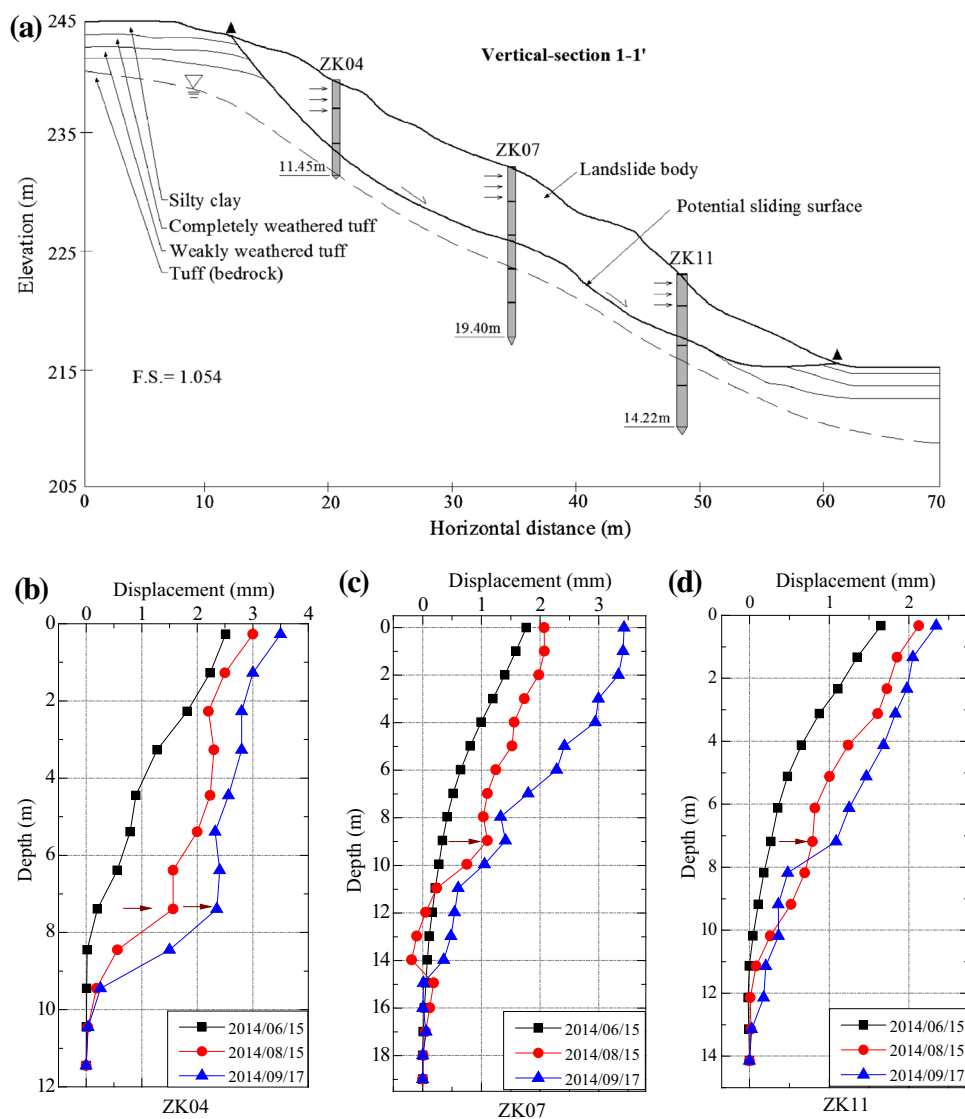
selected. Each vertical section contains three boreholes, and the inclinometers were installed into these boreholes. Generally, ZK03 and ZK04 are located at the slope crest; ZK05, ZK06 and ZK07 are located at the middle of the landslide; and ZK08, ZK10 and ZK11 are located at the bottom. During installation, the U-shaped plane was made parallel to the main sliding direction. In this way, the main movements of the landslide can be measured. The installation of the FBG inclinometers and the following data acquisition are shown in Fig. 5. In addition, meteorological data of Wencheng County show that the average annual rainfall is 1698 mm with a maximum daily rainfall of 256.61 mm, with most rain falling between April and September. Rainfall during this period accounts for more than 50 % of the annual total rainfall. Because the monitoring was in this period, the rainfall was thought to be the main factor that caused the soil mass movements in this landslide.

4 Result analysis

4.1 Monitoring results of FBG-based in-place inclinometer

The first strain data of the FBG sensors were collected on May 23, 2014 as initial data. The following data were collected on June 15, August 15, and September 17,

Fig. 6 **a** Limit equilibrium analysis results for vertical-section 1-1'; **b** displacement profile measured by FBGs at borehole ZK04; **c** displacement profile measured by FBGs at borehole ZK07; **d** displacement profile measured by FBGs at borehole

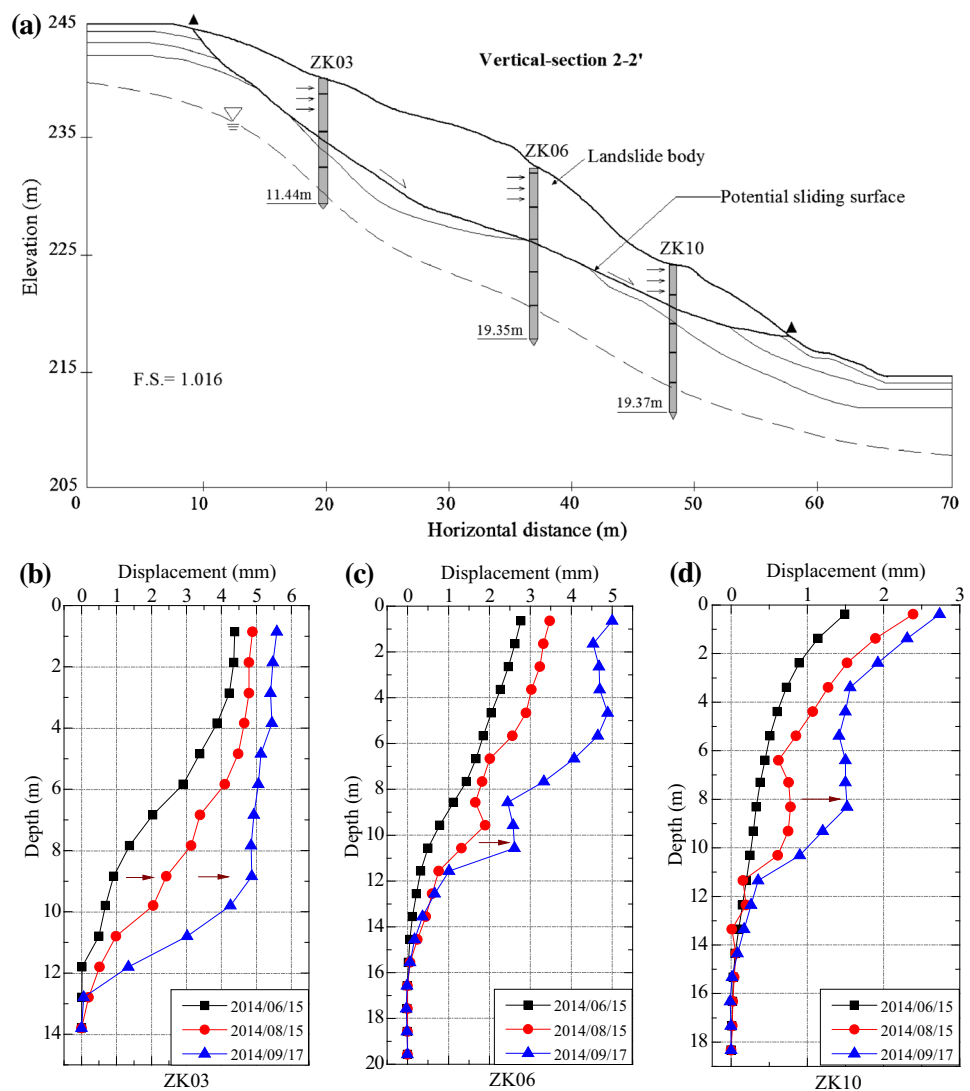


respectively. Figures 6, 7, 8 show the stability analysis results of vertical-section 1-1', 2-2' and 3-3' using LEA, and the displacement profiles measured by the FBG inclinometers. The location of the inclinometers with respect to the potential sliding surfaces is also shown in these figures. The FBG sensors in ZK02 were damaged due to inadequate protection after field installation, so the displacement profile of ZK02 is not available in Fig. 8.

From these figures, it is found that the horizontal displacements increase from the bottom to the surface, indicating that the whole monitored area of the landslide was moving during the period of monitoring. Furthermore, there was a stable area with negligible displacement at the bottom of each borehole. The existence of these stable areas indicates that the boreholes were drilled into stable zones within the bedrock.

ZK03 and ZK04 are located at the crest of the slope; the displacement profiles in these two boreholes are shown in Figs. 7b and 6b. As time went, the soil mass moved slowly at the borehole bottom. And the displacements began to change significantly at the depths of 9 and 7 m for ZK03 and ZK04, respectively. These shift points were near the crust–bedrock interface, which means that the potential sliding surface may pass through this surface. The displacement profiles of ZK05, ZK06 and ZK07 are shown in Figs. 8b, 7c and 6c. These boreholes were located at the middle area of the slope. The shift points of displacements in ZK05, ZK06 and ZK07 were found at the depths of 10.5, 10.5 and 9.0 m, respectively. ZK08, ZK10 and ZK11 were located at the bottom of the slope, and the corresponding displacement profiles are shown in Figs. 8c, 7d and 6d. In general, the displacements of soil mass in ZK08, ZK10 and ZK11 were smaller compared with others

Fig. 7 **a** Limit equilibrium analysis results for vertical-section 2-2'; **b** displacement profile measured by FBGs at borehole ZK03; **c** displacement profile measured by FBGs at borehole ZK06; **d** displacement profile measured by FBGs at borehole ZK10



boreholes, but the shift points of displacements were still found at the depths of 8.5, 8.0 and 7.0 m, respectively. In summary, the movements at the crest and the middle area of the landslide were obviously larger than those at the toe. Since the shift points of displacements are all close to the bedrock surface, it can be concluded that the crust–bedrock surface was the most potential sliding surface within the landslide.

4.2 Limit equilibrium analysis

Although FBG-instrumented inclinometers are able to capture accurate deformations of landslides, the ‘factor of safety’, which is universally used as a measure of proximity of slope conditions to failure, cannot be obtained from the field monitoring data. In addition, geological materials are very complicated, whose properties are affected by internal and external factors, i.e., the

gravitational field and rainfalls. Therefore, these data are local and are easily influenced by the selection procedure of monitoring boreholes. To perform more effective evaluation of the instability of landslides, a combination of FBG technique and numerical analysis is suggested. As a result, this paper utilizes a commercial slope stability analysis software SLOPE/W to calculate the most critical failure surface and the corresponding factor of safety.

The limit equilibrium analysis is based on the method of slices to determine the factor of safety against slope failure. This paper considers simplified rainfall that closely matches the maximum daily rainfall of the slope site. To simulate a given rainfall event, this paper prescribes a fluid flux $q = 10.69$ mm/h (rainfall for 24 h) at the slope ground surface and applies this flux continuously unless a seepage face condition is detected. SLOPE/W calculates pore pressures on the failure surface based on a prescribed phreatic surface, which is the result of a given rainfall.

Fig. 8 **a** Limit equilibrium analysis results for vertical-section 3-3'; **b** displacement profile measured by FBGs at borehole ZK05; **c** displacement profile measured by FBGs at borehole ZK08

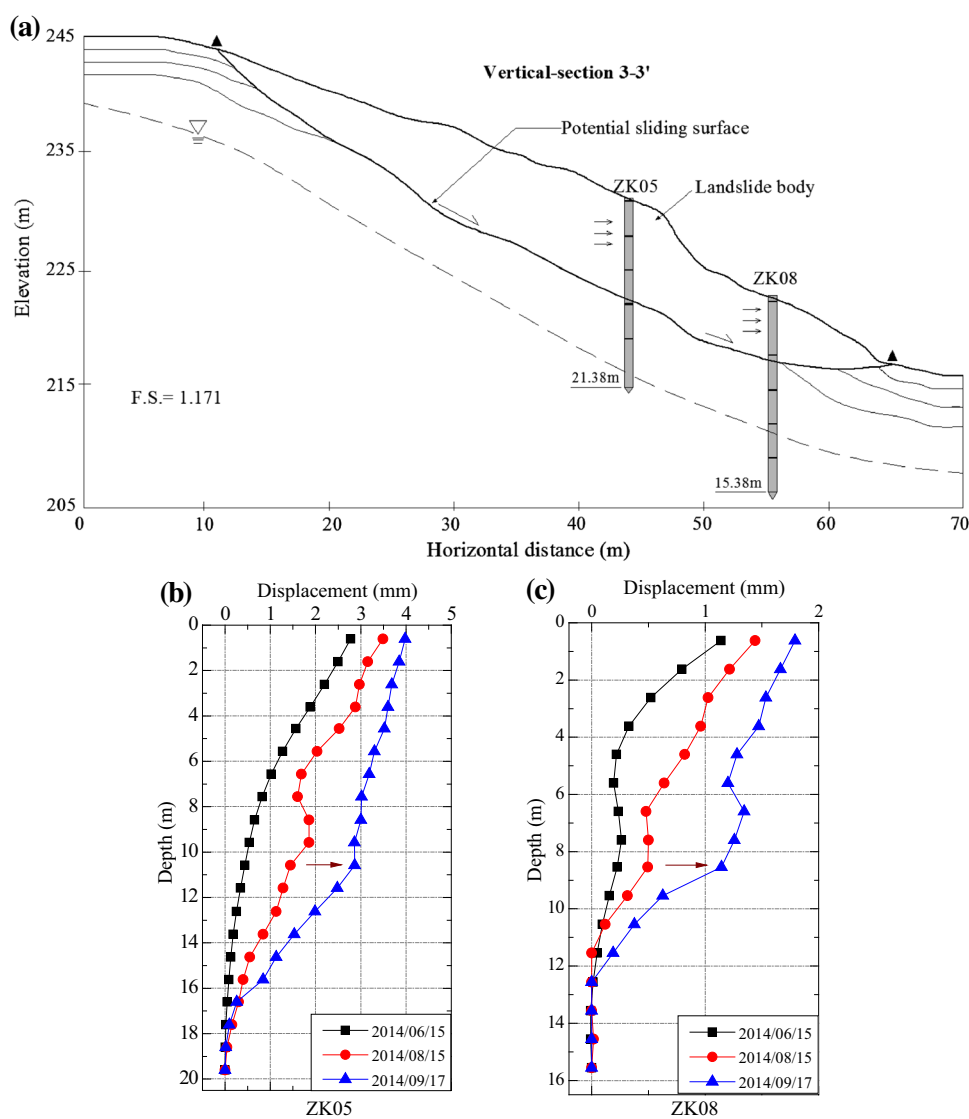


Table 1 Basic parameters of the soil taken from the Wencheng landslide, China

Stratum	h (m)	G_s	w (%)	γ (kN/m ³)	e_0	c (kPa)	φ (°)
Silty clay	0.30–2.40	2.72	27.9	18.7	0.863	21.5	21.0
Completely weathered tuff	1.10–6.20	2.71	25.9	19.3	0.770	21.5	21.0
Weakly weathered tuff	0.80–6.70	2.71	23.4	20.0	0.819	21.5	21.0
Tuff (bedrock)	–	–	–	25.0	–	31.0	26.0

Morgenstern-Price is employed as the method of slope stability analysis. And the auto locate algorithm is selected as the slip surface option in SLOPE/W. The SLOPE/W program models the weathered crusts in the slope as a Mohr–Coulomb material, and assumes the underlying bedrock to be rigid. The relevant material parameters for the four weathered crusts are unit weight γ , cohesion c and dilatancy angle φ , as shown in Table 1. After 24 h, the

critical failure surface was detected to be generally along the crust–bedrock interface. Remarkably, the location of critical sliding areas predicted by FBGs agrees well with the critical slip surface identified by the limit equilibrium methods, suggesting that combination of the two solutions is a meaningful approach for studying the deformation and stability properties of the slope. Furthermore, three vertical sections of the pre-slide geometry are shown in Figs. 6a, 7a

and 8a. The calculated factors of safety of vertical Sects. 1-1', 2-2' and 3-3' are 1.054, 1.016 and 1.171, respectively. As an important supplement to FBGs, LEA indicates that the potential sliding area obtained by FBGs are reasonable, and the slope is overall stable. Here the authors note that the scope of this paper is limited to understanding the timing and relevant triggering mechanism of slope failure for a given rainfall intensity, extreme climate and human activities are not taken into consideration.

5 Conclusions

In this paper, an FBG-based in-place inclinometer was designed and applied to a landslide monitoring project in Wenzhou, China. The displacement of soil mass at different depths within the landslide and its variations with time were accurately captured by FBGs after a four-month period of monitoring. A limit equilibrium analysis (LEA) was also carried out to verify the monitored data. The main findings of the paper can be summarized as follows:

1. The field monitoring data showed that the soil deformations above the bedrock were relatively large whereas those below the bedrock were minor. On this basis, the potential sliding zones were predicted to be the areas near the bedrock.
2. The factor of safety calculated from the LEA was around 1.00, indicating that the landslide is overall stable. Furthermore, the calculated failure surface was consistent with that predicted by the field data.
3. Although FBG-instrumented inclinometers are able to capture accurate deformations of landslides, these data are local and are easily influenced by the selection procedure of monitoring boreholes. To perform more effective evaluation of the instability of landslides, a combination of FBG technique and numerical analysis is suggested.

Acknowledgments This work was financially supported by State Key Program of National Natural Science of China (No. 41230636), National Basic Research Program of China (973 Program) (No. 2011CB710605), National Natural Science of China (Grant No. 41302217), the Evaluation of Geology and Mineral Resources Survey (No. 12120113007800), and Open Fund of State Key Laboratory of Hydraulics and Mountain River Engineering (Grant no. 1209). The authors would also like to thank the technical staff of the Suzhou NanZee Sensing Ltd for their assistance in developing the FBG sensors. Special thanks are given to Cheng-Cheng Zhang, Jing-Hong Wu and Jun-Kuan She, all of Nanjing University, for correcting this paper with respect to written English.

References

1. Iten M, Puzrin AM, Schmid A (2008) Landslide monitoring using a road-embedded optical fiber sensor. In: Proceedings of Conference on Smart Sensor, Phenomena, Technology, Networks, and Systems, 6933(15): 93315–93315
2. Wang BJ, Li K, Shi B, Wei GQ (2009) Test on application of distributed fiber optic sensing technique into soil slope monitoring. *Landslides* 6(1):61–68
3. Huang AB, Lee JT, Ho YT, Chiu YF, Cheng SY (2012) Stability monitoring of rainfall induced deep landslides through pore pressure profile measurements. *Soils Found.* 52:737–747
4. Lienhart W, Woschitz W, Moser F (2014) High sensitive monitoring of natural and engineered slopes. In: Proceedings of 5th International Forum on Opto-electronic Sensor-based Monitoring in Geo-engineering 8–14
5. Zeni L, Picarelli L, Avolio B (2014) Brillouin Optical Time Domain Analysis for geotechnical monitoring. In: Proceedings of 5th International Forum on Opto-electronic Sensor-based Monitoring in Geo-engineering 29–33
6. Sun Y, Zhang D, Shi B, Tong HJ, Wei GQ, Wang X (2014) Distributed acquisition, characterization and process analysis of multi-field information in slope. *Eng Geol* 182(A): 49–62
7. Zhu HH, Shi B, Zhang J, Yan JF, Zhang CC (2014) Distributed fiber optic monitoring and stability analysis of a model slope under surcharge loading. *J Mount Sci* 11(4):979–989
8. Zhu HH, Shi B, Yan JF, Zhang J, Zhang CC, Wang BJ (2014) Fiber Bragg grating-based performance monitoring of a slope model subjected to seepage. *Smart Mater Struct* 23(9):095027
9. Ho YT, Huang AB, Lee JT (2006) Development of a fibre Bragg grating sensed ground movement monitoring system. *Meas Sci Technol* 17(7):1733–1740
10. Pei HF, Yin JH, Zhu HH, Hong CY, Jin W, Xu DS (2012) Monitoring of lateral displacements of a slope using a series of special fibre Bragg grating-based in-place inclinometers. *Meas Sci Technol* 23(2):025007
11. Zhu HH, Ho ANL, Yin JH, Sun HW, Pei HF, Hong CY (2012) An optical fibre monitoring system for evaluating the performance of a soil nailed slope. *Smart Struct Systems* 9(5):393–410
12. Zhang CC, Zhu HH, Shi B, She JK (2014) Interfacial characterization of soil-embedded optical fiber for ground deformation measurement. *Smart Mater Struct* 23(9):095022
13. Zhang CC, Zhu HH, Shi B, Zhang D, She JK (2015) Quantitative evaluation of optical fiber/soil interfacial behavior and its implications for sensing fiber selection. *IEEE Sens J* 15(5):3059–3067. doi:10.1109/JSEN.2014.2386881
14. Kersey AD, Davis MA, Patric HJ, LeBlanc M, Koo KP, Askins CG, Putnam MA, Friebele EJ (1997) Fiber grating sensors. *J Lightwave Technol* 15(8):1442–1463
15. Hao JZ, Tjin SC, Chaudhui PR, Liaw CY, Guo X, Lu C (2003) Realization of an embedded fiber Bragg grating-based pressure sensor in fiber-reinforced composites: embedding techniques and performance characteristics. In: Proceeding of SPIE APOC, vol 5279
16. William WM, James RD, Gerald M (1992) Multiplexing fiber Bragg grating sensors. In: Proceeding of SPIE, vol 1586
17. Pei HF, Yin JH, Jin W (2013) Development of novel optical fiber sensors for measuring tilts and displacements of geotechnical structures. *Meas Sci Technol* 24(9):095202